Nontrivial Topological Features and Griffith's-Phase Behavior in CrFeVGa Probed by Experiment and Theory

Jadupati Nag,[1] P.C. Sreeparvathy,[1] R. Venkatesh,[2] P.D. Babu,[3] K.G. Suresh,[1,*] and Aftab Alam[1,†]

[1] *Department of Physics, Indian Institute of Technology Bombay, Mumbai 400076, India*
[2] *UGC-DAE Consortium for Scientific Research, University Campus, Khandwa Road, Indore 452001, India*
[3] *UGC-DAE Consortium for Scientific Research, Mumbai Centre, BARC Campus, Mumbai 400085, India*

(Received 13 August 2022; revised 12 March 2023; accepted 17 March 2023; published 24 April 2023)

We report a combined theoretical and experimental study of the topological semimetal CrFeVGa with an emphasis on the role of atomic disorder on the magnetoelectronic properties. CrFeVGa belongs to the quaternary Heusler alloy family and crystallizes in the cubic structure with B2 disorder. It is found that the disorder plays a crucial role in quenching the magnetization (net moment $\sim 5 \times 10^{-2}\ \mu_B$ per formula unit) and other anomalies. Ac and dc magnetization data reveal the occurrence of Griffith's-phase-like behavior in the presence of small magnetic clusters with a weak antiferromagnetic or ferrimagnetic ordering. A nonsaturating, linear positive magnetoresistance is observed even at 70 kOe, in a wide temperature range, which is attributed to the quantum linear magnetoresistance arising due to the zero- or small-gap band structure. Hall measurements show some anomalous behavior (including an anomalous Hall conductivity $\sigma_{xy0} = 270$ S cm^{-1} and an anomalous Hall angle of 0.07 at 2 K) with a significant contribution from the semimetallic bands. Hall data analysis also reveals the presence of some non-negligible topological Hall contribution, which is significant at low temperatures. *Ab initio* calculations confirm the topological Weyl behavior of CrFeVGa, which originates from a unique combination of broken time-reversal symmetry and noncentrosymmetry. The nontrivial band topology stems from the p and d states of vanadium, which overlap near the Fermi level. The presence of multi-Weyl points (24 pairs) near the Fermi level causes a large Berry curvature and hence reasonably high anomalous Hall conductivity. The coexistence of so many emerging features in a single material is rather rare and thus opens up new avenues for future topological and spintronics-based research.

DOI: 10.1103/PhysRevApplied.19.044071

I. INTRODUCTION

In the field of spintronics and multifunctional quantum materials, Heusler alloys are being studied ubiquitously due to their promising physical properties and novel application potential. A large number of interesting magnetic materials, such as half-metallic ferromagnets [1], spin-gapless semiconductors [2], bipolar magnetic semiconductors [3], and spin semimetals [4], belong to the Heusler family. Compared to other spintronic materials, Heusler alloys are superior due to their stable structure, high spin polarization, and high ordering temperature, and hence are suitable for various applications. However, these alloys are highly prone to atomic and antisite disorder due to various factors like the electronegativity of the constituent elements, sample preparation conditions, etc. In general, imperfections such as disorder, defects, and impurities in materials modify electronic and magnetic properties. For magnetic materials, such disorder can give rise to complex magnetic and electronic features by altering the original electronic band structure. As such, they are the backbone of many advances, and hence have drawn immense interest in the condensed-matter community. In Heusler alloys, the major interest is to understand the role of atomic disorder on magnetoelectronic properties.

In this paper, we report a combined theoretical and experimental study on a new (XX′YZ) quaternary Heusler alloy (QHA) CrFeVGa with an emphasis on the effect of antisite disorder on magnetic, transport, thermal, and electronic properties. CrFeVGa crystallizes in a cubic structure (space group $F\bar{4}3m$) with robust B2 disorder, which is confirmed by normal x-ray diffraction (XRD) and synchrotron x-ray diffraction (SXRD) measurements. Dc and ac magnetization data reveal no magnetic ordering down to 2 K with a moment $5 \times 10^{-2}\ \mu_B$ per formula unit. Interestingly, the dc susceptibility deviates from the ideal Curie-Weiss law, but shows Griffith's-phase-like (GP-like)

*suresh@phy.iitb.ac.in
†aftab@phy.iitb.ac.in

behavior, which is attributed to the antisite disorder present in the system. The magnetization data indicate the possibility of small magnetic clusters, mediated by the atomic disorder, which give rise to a complex magnetic structure. Magnetoresistance (MR) data indicate nonsaturating linear positive magnetoresistance (LPMR) in a wide temperature range. A careful analysis hints at the zero- or small-gap electronic structure near the Fermi level (E_F) as the origin of the quantum LPMR. Hall data further reveal anomalous behavior, chiefly arising from the contribution of the unique band structure, and support the resistivity and MR findings. Heat-capacity data also support the magnetic and transport behavior.

Our *ab initio* simulation confirms a unique semimetallic feature with high spin polarization. A nontrivial band topology originating from the overlap between the p and d states of vanadium atoms is observed. Spin-orbit coupling (SOC) plays a crucial role in the formation of the multi-Weyl points with ± 1 chirality in the vicinity of E_F. Simulation confirms a high anomalous Hall conductivity (AHC), originating from a large Berry flux contributing to its intrinsic part. The present study highlights the role of atomic disorder in altering the physical properties of a Weyl semimetal (WSM) and hence opens up new directions for future applications of potential semimetals in electronic devices such as those in broadband infrared photodetectors, spin topological field effect transistors, etc. [5]. Moreover, various fascinating properties such as the high mobility, large LPMR, and high AHC value of CrFeVGa offer a lot of promise for other applications, such as high-speed electronics and next-generation spintronics. Apart from this, being a topological semimetal, CrFeVGa may draw immense attraction for next-generation topotronics (future topological electronics) and the spin-momentum locking nature of the topological surface states valuable for future spintronics. With a large Berry curvature near E_F, CrFeVGa can also be efficient for spin-Hall-effect-based devices for the conversion of charge current to spin current [6]. Interestingly, there has been recent theoretical progress in designing and fabricating topological catalysts for real-life applications using robust surface states of topological semimetals, which can help to enhance the surface-related chemical processes of traditional catalysts [7]. Topological semimetals such as CrFeVGa may also be considered as a future promising material along this direction.

II. EXPERIMENTAL DETAILS

Polycrystalline samples of CrFeVGa were synthesized using an arc melting system in a high-purity Ar atmosphere using the stoichiometric amount of constituent elements having a purity of 99.99%. In order to compensate for loss, 2% excess Ga was used. To achieve perfect homogeneity, the samples were melted several times and a weight loss of 0.50% was observed after the final melting. Room-temperature XRD data were taken using Cu $K\alpha$ radiation with the help of a Panalytical X-pert diffractometer to study the crystal structure. For the crystal structure analysis, FullProf Suite software [8] was used. Synchrotron-based powder x-ray diffraction measurements were carried out on well-ground powder samples at the extreme conditions angle dispersive/energy dispersive x-ray diffraction (ECAD/EDXRD) beamline (BL-11) at the Indus-2 synchrotron source, Raja Ramanna Centre for Advanced Technology (RRCAT), Indore, India. Measurements were performed in capillary mode and the capillary was rotated at approximately 150 revolutions per minute to reduce orientation effects. The desired wavelength for angle-dispersive x-ray diffraction experiments was selected from the white light from the bending magnet using a Si(111) channel-cut monochromator. The monochromatic beam was then focused on the sample with a Kirkpatrick-Baez mirror. A MAR345 image plate detector (which is an area detector) was used to collect two-dimensional (2D) diffraction data. The sample-to-detector distance and the wavelength of the beam were calibrated using National Institute of Standards and Technology standards LaB_6 and CeO_2. Calibration, conversion, and/or integration of the 2D diffraction data to one dimension, intensity versus 2θ, were carried out using FIT2D software.

Magnetization measurements at various temperatures were carried out using a vibrating sample magnetometer attached to a physical property measurement system (PPMS) (Quantum Design) for fields up to 60 kOe. ac susceptibility (ACS) measurements were carried out using the ac measurement system option attached to the PPMS in the temperature range of 3–200 K at varying frequencies with an applied ac field of 5 Oe. Temperature- and field-dependent resistivity along with the MR measurements were also carried out using the PPMS, with the help of the electrical transport option in the traditional four-probe method, applying a 10 mA current at 21 Hz frequency. Hall measurements were carried out using the PPMS with the van der Pauw method by applying a 5 mA current at 21 Hz frequency. The thermoelectric power (TEP) in zero magnetic field was measured using the differential dc sandwich method in a homemade setup in the temperature range of 4–300 K.

III. COMPUTATIONAL DETAILS

To study the ground-state structural and magnetic configuration, and the electronic and topological properties of CrFeVGa, *ab initio* calculations were performed using spin-resolved density-functional theory [9] implemented within the Vienna *ab initio* simulation package (VASP) [10–12] with a projected augmented-wave basis [13]. The electronic exchange-correlation potential proposed by Perdew, Burke, and Ernzerhof [14] within the generalized

gradient approximation (GGA) was used. Brillouin-zone integration was done using the tetrahedron method with a $24 \times 24 \times 24$ k-mesh. A plane-wave energy cutoff of 450 eV was used for all the calculations. All the structures were fully relaxed with total energies (forces) converged to values less than 10^{-6} eV (0.01 eV Å $^{-1}$). The Wannier90 [15–17] simulation tool was used to compute the tight-binding Hamiltonian. Further, the WannierTool [18] program was used to examine the topological electronic structure properties such as Weyl points, surface states, Berry curvature, and AHC. To incorporate the B2 disorder, we have generated a 32-atom special quasirandom structure (SQS) [19]. SQS is an ordered structure, known to mimic the random correlation accurately, for disordered compounds. The Alloy Theoretic Automated Toolkit [20] was used to generate the SQS structures. The generated SQS structures perfectly mimic the random pair correlation functions up to third-nearest neighbors.

IV. EXPERIMENTAL RESULTS

A. Crystal structure

1. X-ray diffraction

The quaternary Heusler alloy CrFeVGa crystallizes in the LiMgPdSn prototype structure (space group $F\bar{4}3m$). The experimental lattice parameter was found to be 5.87 Å from the Rietveld refinement. This structure can be seen as four interpenetrating fcc sublattices with Wyckoff positions 4a $(0,0,0)$, 4b $(0.5,0.5,0.5)$, 4c $(0.25,0.25,0.25)$, and 4d $(0.75,0.75,0.75)$. In general, for a XX′YZ QHA, there exist three energetically nondegenerate structural configurations (keeping the Z atom at the 4a site). The three types are

(I) X at 4d, X′ at 4c and Y at the 4b site,
(II) X at 4b, X′ at 4d and Y at the 4c site, and
(III) X at 4d, X′ at 4b and Y at the 4c site.

For a detailed XRD analysis, the structure factor considering configuration type I can be written as [21]

$$F_{hkl} = 4[f_Z + f_Y e^{\pi i(h+k+l)} + f_X e^{(\pi i/2)(h+k+l)} + f_{X'} e^{-(\pi i/2)(h+k+l)}], \quad (1)$$

with different (h,k,l) values. Here f_X, $f_{X'}$, f_Y, and f_Z are the atomic scattering factors for the atoms X, X′, Y, and Z, respectively. For superlattice reflections, (111) and (200), the structure factor can be written as

$$F_{111} = 4[(f_Z - f_Y) - i(f_X - f_{X'})], \quad (2)$$

$$F_{200} = 4[(f_Y + f_Z) - (f_X + f_{X'})]. \quad (3)$$

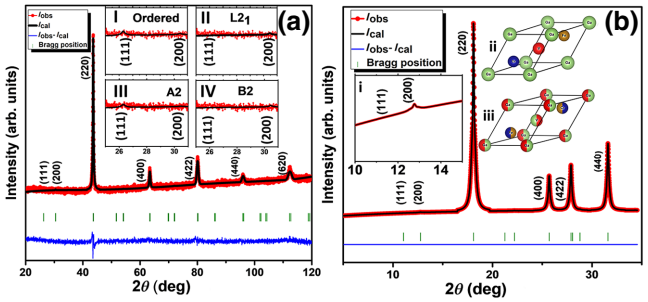

FIG. 1. For CrFeVGa, (a) room-temperature powder XRD pattern and (b) synchrotron XRD pattern, including the Rietveld-refined data for configuration type I with 50% disorder between Cr and Fe, and 50% disorder between V and Ga atoms. Insets (I) to (IV) in panel (a) show enlarged views near the (111) and (200) peaks (superlattice peaks) with ordered structure (Y-type), L2$_1$ structure, A2-type disorder, and B2-type disorder, respectively. Inset (i) in panel (b) shows an enlarged view of superlattice peaks with B2-type disorder; and insets (ii) and (iii) show primitive crystal structures corresponding to the Y-type order and the B2-type disorder, respectively.

Figure 1(a) shows the room-temperature XRD pattern of CrFeVGa along with the Rietveld refinement for configuration type I with 50% disorder between tetrahedral sites, i.e., Cr and Fe (X and X′) atoms, and 50% disorder between octahedral sites, i.e., V and Ga (Y and Z) atoms. As is evident from Fig. 1(a), superlattice peaks are absent, indicating the possibility of disorder in the system. For the constituent elements having almost the same values of scattering factors, it becomes very difficult to identify an accurate structure from conventional XRD. To find out the correct structure, we have performed rigorous structural analysis considering all possible ordered and disordered structures in all the configurations. Insets (I) to (IV) of Fig. 1(a) show enlarged views near the (111) and (200) peaks (superlattice peaks) with ordered structure (Y-type), L2$_1$ structure, A2-type disorder, and B2-type disorder, respectively, for configuration type I (as for the rest of the configurations, XRD did not fit well).

We started with the refinement to the pure configuration as shown in inset (I) of Fig. 1(a), which clearly did not fit well. For L2 $_1$-type [see inset (II) of Fig. 1(a)], refinement considering antisite disorder between V and Ga atoms resulted in $\chi^2 = 1.40$. Refinement considering A2-type disorder (random mixing among all the sites) resulted in $\chi^2 = 2.40$, which also did not fit well [see inset (III) of Fig. 1(a)]. For B2-type disorder, refinement considering 50% antisite disorder between Cr and Fe, and between V and Ga atoms, has been performed for all three configurations. The best fit with the lowest χ^2 (1.30) was found in configuration type I [see inset (IV) of Fig. 1(a)].

As conventional XRD cannot give very accurate structural assessment for this system, we have gone further and carried out SXRD using a synchrotron radiation source

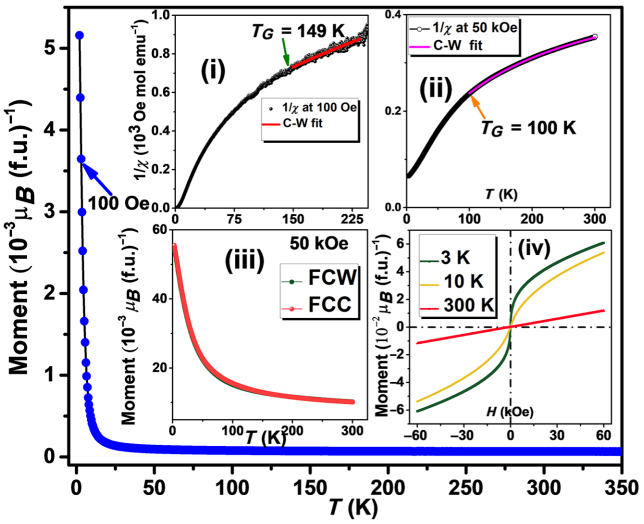

FIG. 2. For CrFeVGa, M vs T in field-cooled cooling (FCC) mode in $H = 100$ Oe. Inset (i) shows the T variation of inverse susceptibility along with the Curie-Weiss fit. Inset (ii) shows the Curie-Weiss fit for $H = 50$ kOe. Inset (iii) shows M vs T curves for FCC and field-cooled warming (FCW) data in 50 kOe. Inset (iv) shows M vs H curves at 3, 10 and 300 K.

($\lambda = 0.6525$ Å) to understand the local atomic order-disorder. The synchrotron XRD pattern along with the Rietveld refinement for configuration type I with B2 disorder is shown in Fig. 1(b). Interestingly, the SXRD data confirm the presence of the (200) superlattice peak [see inset (i) of Fig. 1(b)], indicating the existence of B2-type disorder in this system. Hence, we conclude that CrFeVGa crystallizes in cubic structure with a B2-type disorder with 50% disorder between tetrahedral sites, i.e., Cr and Fe (X and X′) atoms, and 50% disorder between octahedral sites, i.e., V and Ga (Y and Z) atoms. The crystal structure corresponding to the Y-type order and the best fit with B2 disorder are shown in insets (ii) and (iii) of Fig. 1(b).

B. Magnetic properties

Figure 2 and inset (iii) of Fig. 2 show M vs T for CrFeVGa measured at $H = 100$ Oe and $H = 50$ kOe, respectively. The FCC curve taken at $H = 100$ Oe shows a sharp rise below 25 K, whereas both FCC and FCW curves taken at 50 kOe show a monotonic increase below 75 K. This type of sharp rise in the M vs T data indicates the possibility of magnetic ordering at very low T. Inset (iv) of Fig. 2 shows M vs H curves at various T.

The magnetic moments (m) can be calculated by considering the total number of valence electrons (n_v) of the constituent elements [22]. According to the Slater-Pauling rule [23,24], the magnetic moment (m) for a completely ordered alloy is given by

$$m = (n_v - 24)\ \mu_B\ \text{f.u.}^{-1}. \tag{4}$$

CrFeVGa should possess 2.0 μ_B f.u.$^{-1}$ in the fully ordered state. But interestingly, the observed moment turns out to be negligibly small (5×10^{-2} μ_B f.u.$^{-1}$). The presence of B2 disorder can be a plausible reason for the quenching of the moment. The susceptibility data ($H = 100$ Oe) have been fitted (solid red line) above 145 K (the Curie-Weiss law deviates below 150 K) using the Curie-Weiss law, $\chi^{-1} = 1/(\chi_0 + C/(T - \theta_P))$. From the fit, we obtained $\chi_0 = 3.74 \times 10^{-4}$ emu mol^{-1} Oe^{-1} and Weiss temperature $\theta_W = -25$ K. The latter indicates the presence of antiferromagnetic (AFM) interactions in the system. The nonsaturating behavior (even up to 60 kOe field) of the low-T M vs H curves, along with negligible hysteresis and very low moment, indicate superparamagneticlike behavior, possibly attributable to the B2 disorder.

Furthermore, the $1/\chi$ vs T plots [see insets (i) and (ii) of Fig. 2] depict a deviation from the Curie-Weiss behavior below 150 K for $H = 100$ Oe and below 100 K for $H = 50$ kOe, respectively, indicating the possibility of GP-like behavior in this system [25]. We have defined the Griffith's temperature T_G as the temperature at which $1/\chi$ deviates from the Curie-Weiss law. Thus T_G is the highest temperature at which there exists a short-range ferromagnetic (FM) ordering, while the system is completely paramagnetic above T_G. For the $H = 100$ Oe and $H = 50$ kOe data, T_G is 149 K and 100 K, respectively. As the field is increased, T_G decreases, which is a characteristic feature of the Griffith's phase [25]. This is because, at lower fields, the moments of FM clusters can easily prevail over the paramagnetic regime, while the same does not happen at higher fields. Generally, GP is observed in frustrated magnetic systems [25] and rarely seen in Heusler systems. The presence of antisite disorder expedites the possibility of GP in this system, and in turn plays a significant role [26,27], leading to interesting magnetic features. The competition between FM and AFM phases can also be a source of occurrence of GP. The existence of GP-like behavior in CrFeVGa can be explained on the basis of quenched disorder and the coexistence of competing FM and AFM phases [27]. Griffith's singularity [28] is represented by a power law of $1/\chi$ as

$$\chi^{-1} = (T - T_C^R)^{1-\lambda}, \tag{5}$$

where T_C^R is the random critical temperature and λ is the susceptibility exponent ($0 \le \lambda \le 1$), which means the deviation from the Curie-Weiss (CW) behavior. In the paramagnetic regime (above T_G), λ should ideally be zero [28].

Figure 3(a),(b) show fits to our χ^{-1} data [using Eq. (5)] to look into the presence of GP-like behavior. From the fits, we obtained $\lambda = 0.88 \pm 0.05$, which is in good agreement with the expected range of 0 to 1, and comparable to that of other reported systems from the Heusler family [29,30], indicating the presence of GP-like behavior. The calculated

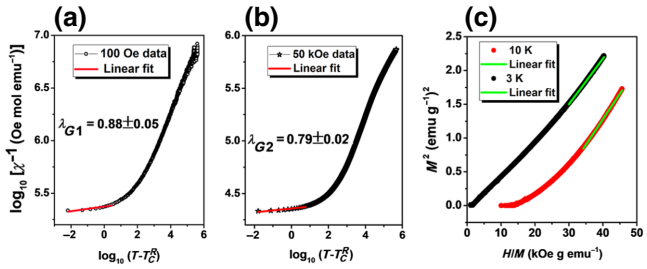

FIG. 3. For CrFeVGa, the power-law fit (solid red line) to χ^{-1} at (a) 100 Oe and (b) 50 kOe according to Eq. (5). (c) Arrott plots at 3 K and 10 K and linear fitting (solid green line).

value of T_C^R is 25 K (as $\theta_{\rm CW}$ is negative in our case, and no magnetic ordering is found down to 2 K, we have approximated $T_C^R = |\theta_{\rm CW}|$) [25], which is also above the ordering temperature. We found $\lambda = 0.88 \pm 0.05$ from fitting the 100-Oe data, which is higher than that for the 50-kOe data ($\lambda = 0.79 \pm 0.02$ for 50 kOe). Thus λ is higher in the lower field, again a characteristic feature of GP-like behavior [25]. To further analyze this behavior in more detail, we have checked the Arrott plots along with a linear fit, as shown in Fig. 3(c). The presence of nonlinear behavior indicates the presence of magnetic inhomogeneities [25] and the absence of any spontaneous magnetization, which again confirms the presence of GP-like behavior.

To further investigate the magnetic properties of CrFeVGa, we have performed frequency-dependent ACS measurements in the range of 3–200 K using ac frequencies of 10 Hz to 9 kHz. Figure 4 shows the T variation of the real (χ') and imaginary (χ'') components of ACS, which agree with the dc magnetization data. The absence of a prominent peak confirms no magnetic ordering down to low T. The absence of any frequency dependence in the ACS data rules out spin-glass nature in this system. Thus, dc and ac magnetization data reveal the possibility of small magnetic clusters in the paramagnetic regime, formed by weakly interacting magnetic moments, where no spontaneous magnetization is observed (as revealed from the Arrott plot). This also confirms the absence of coherent long-range order in this system, because of the atomic disorder.

C. Transport properties

1. Resistivity

Figure 5(a) shows the T dependence of longitudinal resistivity (ρ_{xx}) at zero field and at different fields [see inset (iii) of Fig. 5(a)]. In the low-T region, it is a bad metal, as ρ_{xx} increases with T very slowly. This has also been verified by plotting $\log_2(\rho_{xx})$ vs $\log_2(T)$ in the T range of 18–100 K along with a perfect linear fit [see inset (i) of Fig. 5(a)]. From the fit, we obtained the value of exponent α to be 0.02, which is negligibly small, indicating the

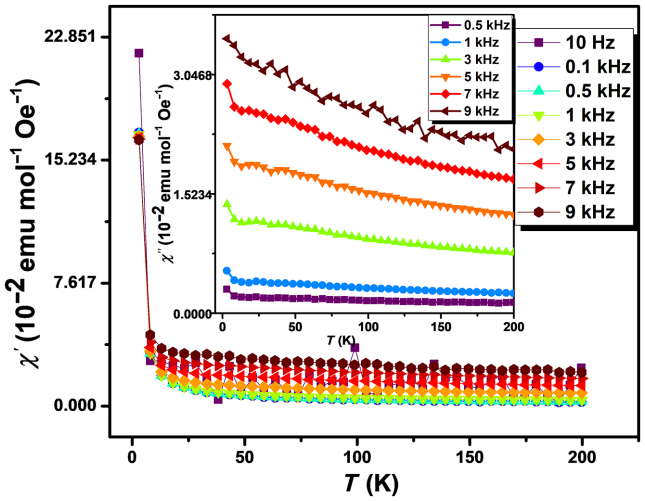

FIG. 4. For CrFeVGa, T variation of ac susceptibility χ' (real part) for various frequencies driven at 5 Oe ac field. The inset shows the T variation of out-of-phase ACS (χ'').

semimetallic nature of CrFeVGa. On the other hand, the resistivity data show a semiconductinglike behavior above a temperature T_m ($\sim$ 200 K) at which ρ_{xx} reaches a maximum, and this maximum could be due to the competition between positive and negative temperature coefficients of resistivity in this disordered alloy, while the effective carrier density remains constant (this is also revealed by the electronic structure calculations shown later) [31].

From the variation of the resistivity data, it appears that, in the high-T regime (200–390 K), semiconductinglike behavior dominates, possibly due to the effect of thermally activated carriers. In the present case, the resistivity increases because the effective carrier density remains constant [also confirmed by constant density of states (DOS) near the Fermi level] and the phonon scattering increases with T. At higher T ($>$ 200 K), the transport becomes activated, and the resistivity decreases with increasing T [32]. The semiconductinglike [negative temperature coefficient of resistivity (TCR)] behavior for $T > 200$ K is attributed to the disorder and/or point defects. For clean systems (pure metal and alloys), resistivity behavior is dominated by phonon scattering (increase in resistivity with T) following the semiclassical Boltzmann transport. But in a disordered alloy (such as CrFeVGa), the resistivity behavior deviates from the conventional classical behavior reflecting sign change of TCR.

In order to further investigate the transport nature, we have fitted the conductivity data with a modified two-carrier model, Eq. (7) [33,34] (in the T range of 200–390 K). This is shown in inset (ii) of Fig. 5(a).

We have considered the two-carrier model, for which

$$\sigma(T) = e(n_e\mu_e + n_h\mu_h), \tag{6}$$

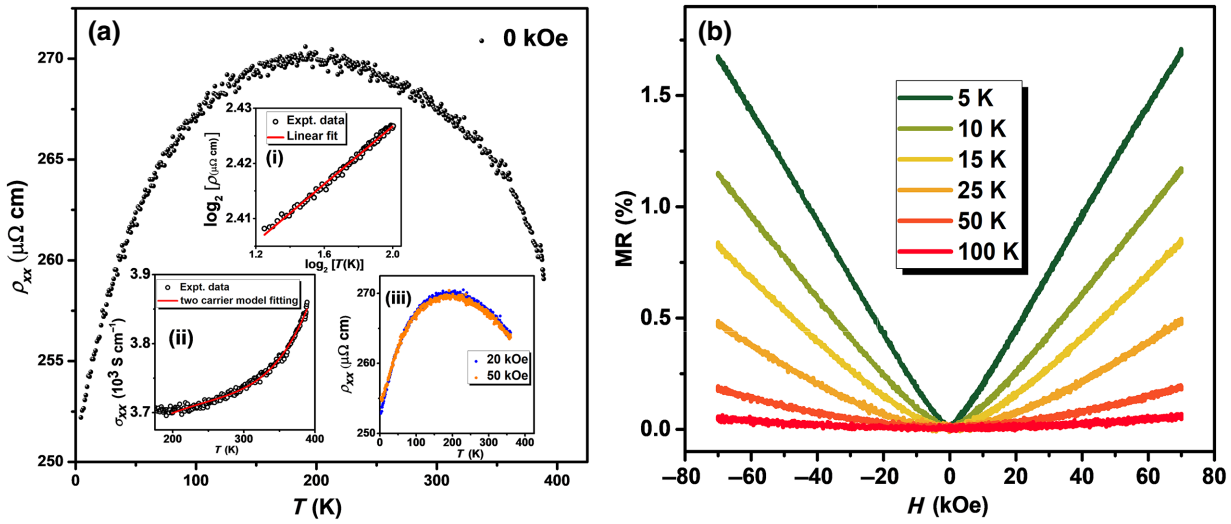

FIG. 5. For CrFeVGa, (a) longitudinal resistivity (ρ_{xx}) vs T in zero field. Inset (i) shows the $\log_2(\rho_{xx})$ vs $\log_2(T)$ plot fitted in the T range of 18–100 K at 0 kOe. Inset (ii) shows the longitudinal conductivity (σ_{xx}) vs T in zero field along with a two-carrier model fit [Eq. (7)] in the semiconducting regime (200–390 K). Inset (iii) shows ρ_{xx} vs T at two different fields. (b) Plot of MR vs H at various temperatures in the T range of 5–100 K.

where $n_i = n_{i0}e^{-\Delta E_i/k_BT}$ $(i = e, h)$ are the electron and hole carrier concentrations, and μ_i, and ΔE_i are the mobilities and pseudogaps, respectively. Equation (6) can be written as

$$\sigma(T) = [A_e(T)e^{-\Delta E_e/k_BT} + A_h(T)e^{-\Delta E_h/k_BT}]. \qquad (7)$$

From the two-carrier model fitting, the energy gaps (ΔE_i) turn out to be negligibly small.

2. Magnetoresistance

Another interesting feature of the present system is the observation of nonsaturating LPMR in a wide T range. Figure 5(b) shows MR vs H at different T, where the MR ratio is defined as $R_M(H) = \{[\rho(H) - \rho(0)]/\rho(0)\} \times 100\%$. MR increases with H in a perfectly linear fashion in the entire field range, and the low-temperature MR is still linear at 70 kOe. At 3 K, we have obtained $\sim 4\%$ MR at $H = 70$ kOe, which is remarkably high in a disordered system as compared to other reported systems [35,36]. The slope of the linear region decreases with increasing T, and, above 100 K, the magnitude of MR becomes very small ($\sim 0.01\%$ at 300 K). The occurrence of LPMR is indeed anomalous, as the $R_M(H)$ dependence is usually quadratic with H. The origin of such a feature is ambiguous, and it may arise due to several reasons, e.g., (i) disorder-mediated mobility fluctuations [32], (ii) quantum linear MR behavior in the zero- or small-gap electronic band structure near E_F [37,38], etc. For CrFeVGa, LPMR possibly arises due to the second reason [36]. Such large nonsaturating LPMR can be quite promising for high-speed electronics and next-generation spintronic devices. As the origin of LPMR depends mainly on the mobility and carrier concentration parameters, we have further investigated the Hall effect as described below.

3. Hall measurements

Interestingly, the Hall resistivity (the MR contribution is removed using the expression $\rho_{xy} = [\rho_{xy}(H) - \rho_{xy}(-H)]/2$) also shows several anomalies such as (1) a characteristic humplike feature in topological Hall effect (THE) data (maximum at 2 K), (2) nonlinear behavior at low fields while linearity is observed at higher fields, (3) switch of sign from negative to positive at low field and low T, and (4) a crossover from p-type to n-type character [see Figs. 6(a)–6(d)]. To better understand these anomalies, we have considered the empirical Hall resistivity expression for a magnetic material as

$$\rho_{xy} = \rho_{xy}^N + \rho_{xy}^A = R_0H + R_AM, \qquad (8)$$

where ρ_{xy}^N and ρ_{xy}^A are the normal and the anomalous Hall effect resistivity (AHE) contributions, and R_0 and R_A denote the ordinary and anomalous Hall coefficients, respectively. The AHE contribution can be scaled as $\rho_{xy}^A = S_A\rho_{xx}^2M$, where S_A is independent of field and ρ_{xx} is the longitudinal resistivity.

We have experimentally observed a reasonably large anomalous Hall conductivity ($|\sigma_{xy}^A| = \rho_{xy}/(\rho_{xy}^2 + \rho_{xx}^2)$) of 270 S cm^{-1} at 2 K, as shown in Fig. 7(d). We also estimated the carrier concentration $n = 1.26 \times 10^{19}$ cm^{-3} at 2 K, which is in the same order as the narrow-gap semiconductor or semimetal carrier density. To further quantify the

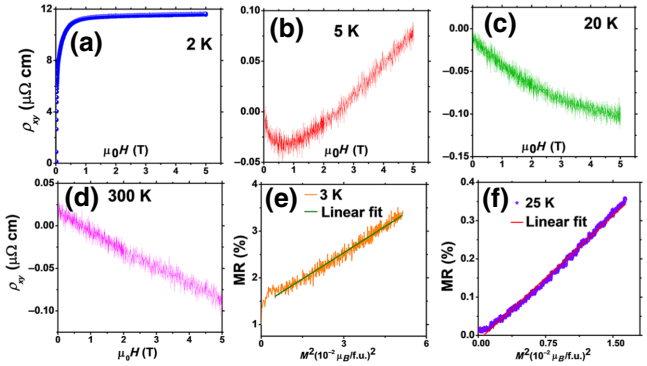

FIG. 6. For CrFeVGa, (a)–(d) Hall resistivity (ρ_{xy}) vs H at 2, 5, 20, and 300 K, respectively. (e),(f) Plots of MR vs M^2 with linear fit (solid line) at 3 and 25 K, respectively.

AHE, we have used another scaling parameter, the anomalous Hall angle, defined as $\sigma_{xy}^A/\sigma_{xx} = (\sigma_{xy} - \sigma_{xy}^N)/\sigma_{xx}$. The maximum value of the AHA reaches 0.07, as shown in the inset of Fig. 7(d). This AHA value is remarkably high among bulk materials [39], as compared to other single-crystal systems, such as Mn_3Sn (AHA ≤ 0.02) [40], and in line with Mn_3Ge (AHA ~ 0.05) [41].

However, ρ_{xy} was found to deviate from the Hall resistivity fit of Eq. (8), as shown in Figs. 7(a) and 7(b). This

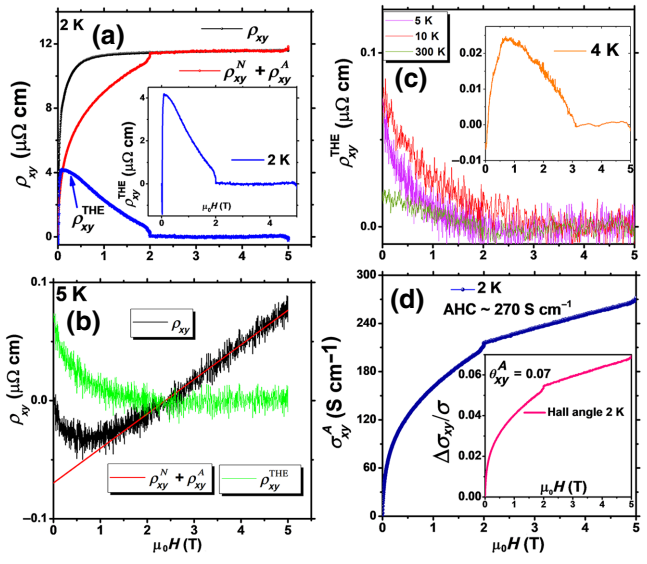

FIG. 7. For CrFeVGa, (a) total Hall resistivity (ρ_{xy}) vs H at 2 K (black curve). The red curve shows the sum of the normal and anomalous Hall contributions, while the blue curve indicates the topological Hall contribution (ρ_{xy}^{THE}). Notice the change of sign in ρ_{xy}^{THE} at about 2 T. (b) Plot of ρ_{xy} vs H at 5 K along with the normal, anomalous, and topological Hall contributions. (c) Plot of ρ_{xy}^{THE} vs H at 5, 10, and 300 K. The inset shows ρ_{xy}^{THE} vs H at 4 K. (d) AHC (σ_{xy}^A) vs H at 2 K. The inset shows the anomalous Hall angle (AHA) vs H.

clearly hints toward the existence of an additional contribution, namely the topological Hall effect ρ_{xy} [42]. Hence, the total Hall resistivity is expressed as

$$\rho_{xy}(T) = \rho_{xy}^N + \rho_{xy}^A + \rho_{xy}^{THE} = R_0 H + S_A \rho_{xx}^2 M + \rho_{xy}^{THE}, \tag{9}$$

where ρ_{xy}^{THE} is the topological Hall resistivity. To scale the AHE and THE contributions, we have performed a linear fit to the ρ_{xy}/H vs $\rho_{xx}^2 M/H$ curve in the high-field regions, as THE vanishes at a high H value. From this fitting, the parameters R_0 and S_A are obtained, and THE is extracted by subtracting $\rho_{xy}^N + \rho_{xy}^A$ from Eq. (9) [43]. This ρ_{xy}^{THE} component is shown in Figs. 7(a) and 7(b).

In addition, ρ_{xy}^{THE} vs H at various T is shown in Fig. 7(c). From these fits, a large THE contribution ($\sim 4\ \mu\Omega$ cm) was observed at 2 K. The amplitude of THE decreases rapidly with T, but its contribution was found to exist over a wide T range. The presence of a humplike maximum [44] and sign switching [45] are typical signatures of THE in topological systems [43]. The origin of this may be attributed to the existence of some spin texture [42] and/or the nontrivial band topology near E_F, associated with the complex magnetic structure of this system mediated by atomic disorder. The sign change in ρ_{xy}^{THE} mainly arises due to the spin-chirality fluctuations related to the fictitious magnetic field of the spin textures [46]. Furthermore, the presence of complex magnetic texture is also supported by the linear fit of MR vs M^2 [45] [see Figs. 6(e) and 6(f)].

4. Specific heat

Figure 8 shows the specific heat C_p vs T for various applied fields. The low-T C_p data have been fitted with the equation $C(T) = \gamma T + \beta T^3$, where the first and second terms indicate the electronic and the low-T phonon contributions to C_p, respectively. Inset (i) shows the linear fit of zero-field C_p data while inset (ii) shows a C_p/T vs T^2 plot. The Sommerfeld coefficient, $\gamma = 0.0194$ J mol^{-1} K^{-2}, is obtained from this fit. We have then extracted the density of states at the Fermi level, $n(E_F) \sim 0.5$ states eV^{-1} f.u.$^{-1}$, using the equation $n(E_F) = 3\gamma/(\pi^2 k_B^2)$ [4]. This value matches fairly well with the simulated DOS value (described in the next section). This is also in good agreement with the small semimetallic DOS value near E_F reported for other semimetals, and hence supports our transport and theoretical findings. From the fitting, the Debye temperature is found to be $\theta_D = 254$ K using $\beta = 1.188 \times 10^{-4}$ J mol^{-1} K^{-4}. Interestingly the C_p/T vs T^2 curve shows a shallow minimum in the low-T region, which vanishes with the field [see inset (ii) Fig. 8]. The existence of a possible spin texture may be the reason for the anomalous low-temperature behavior of C_p.

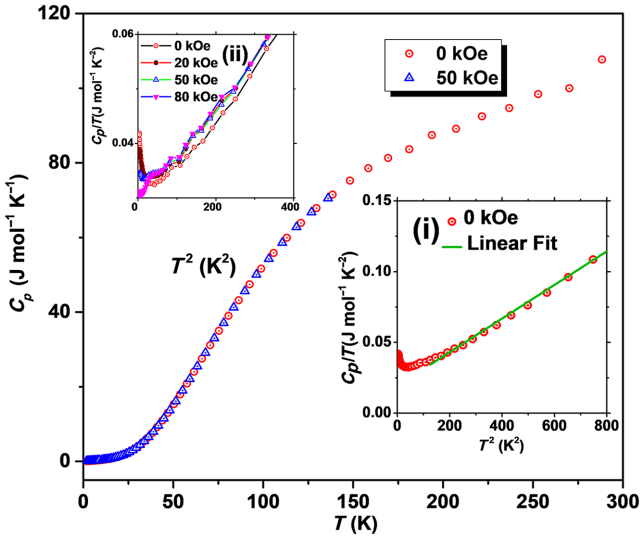

FIG. 8. For CrFeVGa, specific heat (C_p) vs T for 0 and 50 kOe fields. Insets (i) and (ii) show a linear fit (solid green line) for 0 kOe data and the C_p/T vs T^2 plot at various field values, respectively.

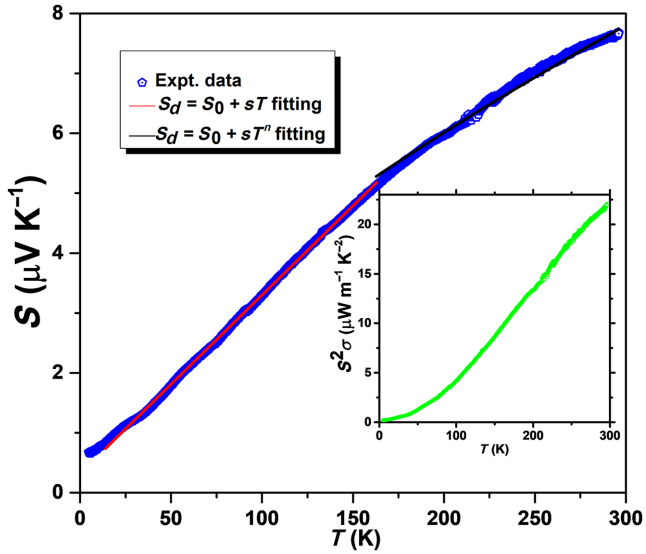

FIG. 9. For CrFeVGa, thermoelectric power S vs T along with a linear fit in the T range of 20–150 K. The inset shows the power factor $S^2\sigma$ vs T.

5. *Thermoelectric power*

Figure 9 shows the T dependence of the TEP S for CrFeVGa. It shows a perfect linear dependence until 150 K, beyond which there is a slight change in the slope, which resembles the changeover in the resistivity data. The positive slope indicates a dominant hole transport outweighing electron transport. The linear variation of S suggests a dominant contribution of diffusion thermopower, which is very similar to other reported narrow-band-gap semiconductors [47]. The magnitude of S is in line with that of other reported semiconducting systems [3], but differs from that of intrinsic semiconductors, for which the magnitude is much higher [47]. However, in small- or zero-gap semiconductors, E_F can switch to the valence band (VB) or conduction band (CB) in one of the spin channels (with a very small gap) due to excitation or impurity states. This leads to a low S value and a slow linear variation of S with T [3]. For small-gap semiconductors such as spin-gapless semiconductors or bipolar magnetic semiconductors, the Seebeck values are reported to be small (1–7 μV K^{-1}) and found to vary linearly with T [3].

In contrast, for typical (intrinsic) semiconductors, S values are larger with a nonlinear variation with T as E_F lies within the band gap. However, for nondegenerate or semiconductors with a small gap in one of the spin channels (as seen in various spin-gapless semiconductors as well as our CrFeVGa), the Fermi level can pierce into the valence or the conduction band of one of the spin channels due to thermal excitation or impurities, leading to a small difference between the DOS just above and below the Fermi level [48]. This makes the Seebeck value small in magnitude. To find out the DOS and carrier density near E_F, TEP data have been fitted with the following equation in the two T ranges (20–150 K and 150–300 K),

$$S_d = S_0 + sT^n, \tag{10}$$

where S_d is the diffusion thermopower, S_0 is a constant, and the slope $s = \pi^2 k_B^2/3eE_F$. From these fits, we obtained E_F to be 0.8 eV (20–150 K) and 0.2 eV (150–300 K) with $n = 1.0$ and $n = 0.7$ in the two T ranges, respectively. The inset of Fig. 9 shows the T dependence of the power factor ($S^2\sigma$) [49].

V. THEORETICAL RESULTS

To study the electronic structure of CrFeVGa, we first simulated the energetics of various structural and magnetic states including ferro-, antiferro-, and ferrimagnetic configurations. Of these, configuration type I with ferrimagnetic order turns out to be energetically the most stable one. Table I shows the simulated results for the theoretically optimized lattice parameters (a_0), atom-projected local moments, and total energy for a few of the lowest-energy configurations. Figure 10 shows the spin-resolved band structure and density of states for configuration type I with ferrimagnetic disorder. A negligible overlap between the CB and VB, and the presence of negligibly small DOS at E_F, indicate a weak semimetallic behavior in this system. Interestingly, we observe the occurrence of topological nontrivial bands and Weyl points near E_F around the X point, as highlighted by the red dashed rectangle in Fig. 10(a) (more details are given below). In the majority-spin channel, small hole pockets appear with a small band

TABLE I. For CrFeVGa, relaxed lattice parameter a_0, atom-projected and total magnetic moments m, and relative energy ΔE for configuration types I, II, and III (with respect to configuration type I) within the GGA approximation.

Type	a_0 (Å)	m^{Co} (μ_B)	m^{Fe} (μ_B)	m^{V} (μ_B)	m^{total} (μ_B)	ΔE (eV f.u.$^{-1}$)
I	5.88	1.83	0.88	−0.75	1.94	0
II	5.85	−0.96	1.29	1.56	1.91	0.54
III	5.93	2.39	1.98	−0.5	3.8	0.64

gap (∼ 0.05 eV) very close to the E_F at the Γ point. Disorder can play a crucial role to push the E_F towards the VB or CB, which can impact the overall electronic structure of the material.

It is worth mentioning that the DOS remains almost unchanged in the energy range of −50 to 50 meV, as shown in the inset of Fig. 10(b). This may arise due to the constant carrier density in the vicinity of E_F [31]. Theoretically, the relaxed lattice parameter ($a_0 = 5.88$ Å) matches fairly well with the experimental value ($a_0 = 5.87$ Å). We have obtained a simulated net moment of $\sim 2\ \mu_B$ f.u.$^{-1}$, which does not follow the experimentally measured value. This difference can be attributed to the B2 disorder present in the system.

To further investigate the semimetallic nature, we have performed band-structure calculations considering the effect of SOC. Figure 11(a) shows the atom and orbital projected band structure of CrFeVGa with SOC. Because of the effect of SOC, the bands around the X point split. This splitting mediates a tiny gap opening along the X-U high-symmetry direction and slight overlap between the VB and CB [see enlarged Fig. 11(b)], which reconfirms the semimetallic nature of CrFeVGa.

The interesting band profile around the Fermi level inspired us to further inspect the topological properties of CrFeVGa. It is apparent that the combination of broken time-reversal symmetry and the noncentrosymmetric nature of CrFeVGa allow the possibility of occurrence of Weyl nodes in the bulk band structure. In order to examine the nontrivial band topology, we have considered the p and d projected electronic band structure, as shown in Fig. 11. In CrFeVGa, the band inversion stems from the overlapping of vanadium p and d states around the X point. The search for nodal points in the entire Brillouin zone revealed 24 pairs of Weyl points near the Fermi level with ±1 chirality. The vanishing of the net chirality value is in agreement with the Nielsen-Ninomiya theorem [50].

Figure 12(a) shows the band dispersion around one such Weyl point. A highly linearized dispersive band nature is evident. Such a topologically nontrivial feature can be useful for several applications such as those in spin topological field effect transistors, broadband infrared photodetectors and topotronics. Further, we have examined the Berry curvature in the k_x-k_y plane, as shown in Fig. 12(b). Clearly, the magnitude of the Berry flux is significantly high, which is possibly due to the existence of multiple Weyl points near the Fermi level that act as the source or sink of the Berry curvature. The surface states originating from the bulk nontrivial band crossing are one of the important parameters in topological materials, which are ideally protected against small external perturbations. Figure 12(c) shows the surface state projected on the (001) surface originating from one of the Weyl points. Such robust surface states can help to enhance the surface-related chemical processes of traditional catalysts [7].

In the vicinity of the Fermi level, one can observe the contributions of other surface states and arc, which arises from other Fermi pockets in the band structure of

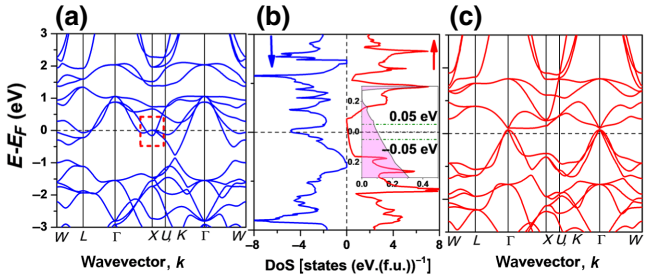

FIG. 10. For CrFeVGa, spin-polarized band structure and density of states at the relaxed lattice parameter (a_0) for configuration type I with ferrimagnetic ordering. The red dashed rectangle in panel (a) highlights the topological nontrivial bands and Weyl node near the E_F at and around the X point. An enlarged view of the DOS near E_F is highlighted in the inset of panel (b).

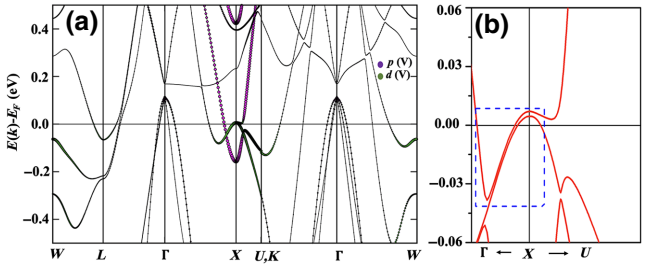

FIG. 11. For CrFeVGa, (a) atom and orbital projected band structure including spin-orbit coupling (SOC) for configuration type I of CrFeVGa. Vanadium p (d) states are shown by green (violet) color. (b) Enlarged view of the band structure around the X-point highlighting the slight overlap of the VB and CB near E_F, confirming the semimetallic nature of CrFeVGa.

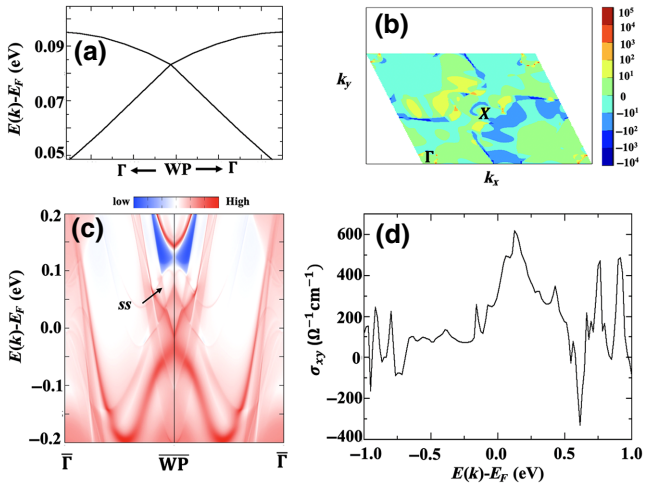

FIG. 12. For CrFeVGa, (a) energy dispersion around a Weyl point, (b) simulated Berry curvature in the k_x-k_y plane at the Fermi level, (c) surface spectra around the Weyl point on the (001) surface, where *ss* stands for surface state, and (d) energy-dependent AHC (σ_{xy}).

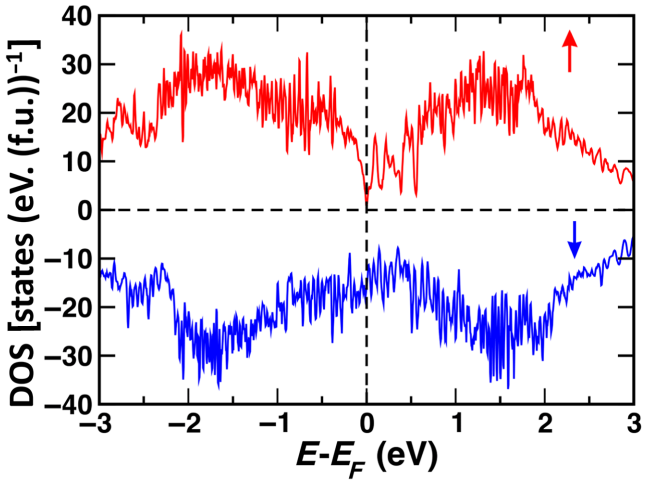

FIG. 13. Spin-polarized density of states for CrFeVGa with B2 disorder (i.e., 50% disorder between Cr and Fe atoms, and 50% disorder between V and Ga atoms).

CrFeVGa. Magnetic WSMs are well known for anomalous transport behavior. In order to check that, we have calculated the intrinsic contribution of AHC originating from the topological Berry curvature. Since the magnetization of the alloy is directed along the z direction, one needs to analyze the transverse conductivity parameter (σ_{xy}). We have simulated the AHC using the equation

$$\sigma_{xy} = -\frac{e^2}{\hbar}\sum_n \int_{\mathrm{BZ}} \frac{d^3k}{(2\pi)^3} f_n(k)\Omega_{n,z}(k),$$

where $f_n(k)$ is the Fermi-Dirac distribution function, and $\Omega_{n,z}(k)$ is the z component of the Berry curvature for the nth band. Our AHC is calculated at 0 K, and hence $f_n(k) = 1$.

Figure 12(d) shows the calculated energy-dependent AHC for CrFeVGa. As expected, the magnitude of AHC in the vicinity of the Fermi level is significantly high ($\sigma_{xy}(E_F) \sim 305\ \Omega^{-1}\ \mathrm{cm}^{-1}$), which is in good agreement with the experimentally obtained AHC value ($\sim 270\ \Omega^{-1}\ \mathrm{cm}^{-1}$). Further, along the positive side of energy, the AHC value is found to increase and attain a maximum value of 616 $\Omega^{-1}\ \mathrm{cm}^{-1}$ at 0.12 eV. Such a high AHC value for CrFeVGa is comparable with other reported topological materials in the literature [51,52], and can be useful for different applications, e.g., spin topological field effect transistors, topotronics, etc.

As mentioned earlier, magnetization measurements yield negligibly small moment for CrFeVGa, which may arise due to the B2 disorder, as confirmed from our experimental XRD data. In order to check it, we have simulated the effect of B2 disorder (fully homogeneous 50% disorder between tetrahedral sites, i.e., Cr and Fe atoms, and between octahedral sites, i.e., V and Ga atoms) on the electronic and magnetic properties of CrFeVGa. For this, we generated special quasirandom structures [19] corresponding to the energetically most favorable type I ordered configuration (see Table I). Figure 13 shows the spin-polarized DOS for this SQS structure. Interestingly, the disordered phase also shows a semimetal behavior for CrFeVGa, with finite DOS in one spin channel and almost zero gap in the other. Energetically, this phase differs only by a few millielectronvolts per formula unit as compared to its corresponding ordered counterpart. The disordered phase, however, gives a much smaller net magnetization ($\sim 0.2\ \mu_B$), which is in accordance with the experimental finding.

Further, we have also simulated the electronic structure of the B2 disordered phase using a 64-atom SQS unit cell. The DOS remains almost the same, but the net moment reduces further to $\sim 0.11\ \mu_B$, in better agreement with the measured value.

VI. SUMMARY AND CONCLUSION

We report a topological semimetallic system, CrFeVGa, which belongs to the quaternary Heusler alloy family. CrFeVGa crystallizes in a cubic structure with 50% B2 disorder between tetrahedral sites, i.e., Cr and Fe atoms, and between octahedral sites, i.e., V and Ga atoms, as confirmed by the synchrotron XRD measurement. We have used a combined theoretical and experimental study to investigate the effect of atomic disorder on the structural, magnetic, transport, electronic, and topological properties of this alloy. B2 disorder is found to play a crucial role in the electronic and magnetic behavior of the system and possibly gives rise to the quenching of moment (∼

5×10^{-2} μ_B f.u.$^{-1}$) and other anomalies. ac and dc magnetization data indicate that the antiferromagnetic interaction between ferrimagnetic clusters is responsible for the Griffith's-phase-like behavior, which eventually leads to anomalous magnetic transition. A nonsaturating linear positive magnetoresistance is observed till 70 kOe, in a wide temperature range, which possibly originates from a quantum linear MR feature in the zero- or small-gap electronic band structure near E_F. Hall measurements support the transport data and display a few anomalies, which were further explained by the simulated band structure of the alloy. A low-temperature anomaly in the specific heat data supports the possible existence of spin texture, as also observed in Hall measurements. *Ab initio* density-functional calculations reveal the topological nontrivial features, including band inversion, Weyl points, and large Berry curvature for pristine CrFeVGa. The simulated value of the intrinsic anomalous Hall conductivity of CrFeVGa matches fairly well with the experiment, and is found to originate mainly from the large Berry flux. Simulation of the special quasirandom structure confirms the B2 disorder as being mainly responsible for the quenching of net magnetization. The present study is crucial to get an insight into the effect of inhomogeneous phases on the critical behavior of weak magnetically ordered systems. The coexistence of different and emerging features such as topological band structure, possible spin texture, large LPMR, and high AHC value in a single material is remarkable, and opens up new frontiers for future topological and spintronics-based research.

ACKNOWLEDGMENTS

J.N. acknowledges the financial support provided by IIT Bombay. J.N. also thanks Dr. Velaga Srihari, ECXRD beamline, BL-11, Indus-2, RRCAT, for carrying out anomalous XRD measurements. The authors thank Dr. Manoj Raama Varma, National Institute for Interdisciplinary Sciences and Technology (CSIR), Thiruvananthapuram, India, for ACS measurements, and Dr. Durgesh Singh for setting up TEP measurements. J.N. and P.C.S thank IIT Bombay Spacetime computing facility. K.G.S. thanks DST-SERB (Grant No. CRG/2020/005589). A.A. acknowledges DST-SERB (Grant No. CRG/2019/002050) for funding to support this research.

[1] R. A. de Groot, F. M. Mueller, P. G. van Engen, and K. H. J. Buschow, New Class of Materials: Half-Metallic Ferromagnets, Phys. Rev. Lett. **50**, 2024 (1983).

[2] Lakhan Bainsla, A. I. Mallick, M Manivel Raja, A. K. Nigam, B. S. D. Ch. S. Varaprasad, Y. K. Takahashi, Aftab Alam, K. G. Suresh, and K. Hono, Spin gapless semiconducting behavior in equiatomic quaternary CoFeMnSi Heusler alloy, Phys. Rev. B **91**, 104408 (2015).

[3] Jadupati Nag, Deepika Rani, Jiban Kangsabanik, Durgesh Singh, R. Venkatesh, P. D. Babu, K. G. Suresh, and Aftab Alam, Bipolar magnetic semiconducting behavior in VNbRuAl, Phys. Rev. B **104**, 134406 (2021).

[4] Y Venkateswara, S Shanmukharao Samatham, P. D. Babu, K. G. Suresh, and Aftab Alam, Coexistence of spin semimetal and Weyl semimetal behavior in FeRhCrGe, Phys. Rev. B **100**, 180404 (2019).

[5] An-Qi Wang, Xing-Guo Ye, Da-Peng Yu, and Zhi-Min Liao, Topological semimetal nanostructures: From properties to topotronics, ACS Nano **14**, 3755 (2020), pMID: 32286783.

[6] Jairo Sinova, Sergio O. Valenzuela, J. Wunderlich, C. H. Back, and T. Jungwirth, Spin Hall effects, Rev. Mod. Phys. **87**, 1213 (2015).

[7] Hua Chen, Wenguang Zhu, Di Xiao, and Zhenyu Zhang, CO Oxidation Facilitated by Robust Surface States on Au-Covered Topological Insulators, Phys. Rev. Lett. **107**, 056804 (2011).

[8] Juan Rodríguez-Carvajal, Recent advances in magnetic structure determination by neutron powder diffraction, Physica B **192**, 55 (1993).

[9] Pierre Hohenberg and Walter Kohn, Inhomogeneous electron gas, Phys. Rev. **136**, B864 (1964).

[10] Georg Kresse and Jürgen Furthmüller, Efficient iterative schemes for *ab initio* total-energy calculations using a plane-wave basis set, Phys. Rev. B **54**, 11169 (1996).

[11] Georg Kresse and Jürgen Furthmüller, Efficiency of ab-initio total energy calculations for metals and semiconductors using a plane-wave basis set, Comput. Mater. Sci. **6**, 15 (1996).

[12] Georg Kresse and Jürgen Hafner, *Ab initio* molecular dynamics for liquid metals, Phys. Rev. B **47**, 558 (1993).

[13] Georg Kresse and Daniel Joubert, From ultrasoft pseudopotentials to the projector augmented-wave method, Phys. Rev. B **59**, 1758 (1999).

[14] John P. Perdew, Kieron Burke, and Matthias Ernzerhof, Generalized Gradient Approximation Made Simple, Phys. Rev. Lett. **77**, 3865 (1996).

[15] Nicola Marzari and David Vanderbilt, Maximally localized generalized Wannier functions for composite energy bands, Phys. Rev. B. **56**, 12847 (1997).

[16] Ivo Souza, Nicola Marzari, and David Vanderbilt, Maximally localized Wannier functions for entangled energy bands, Phys. Rev. B **65**, 035109 (2001).

[17] Nicola Marzari, Arash A. Mostofi, Jonathan R. Yates, Ivo Souza, and David Vanderbilt, Maximally localized Wannier functions: Theory and applications, Rev. Mod. Phys. **84**, 1419 (2012).

[18] QuanSheng Wu, ShengNan Zhang, Hai-Feng Song, Matthias Troyer, and Alexey A. Soluyanov, Wanniertools: An open-source software package for novel topological materials, Comput. Phys. Commun. **224**, 405 (2018).

[19] Alex Zunger, S.-H. Wei, L. G. Ferreira, and James E. Bernard, Special Quasirandom Structures, Phys. Rev. Lett. **65**, 353 (1990).

[20] A. Van de Walle, P. Tiwary, M. De Jong, D. L. Olmsted, M. Asta, A. Dick, D. Shin, Yi Wang, L.-Q. Chen, and Z.-K. Liu, Efficient stochastic generation of special quasirandom structures, Calphad **42**, 13 (2013).

[21] Jadupati Nag, Deepika Rani, Durgesh Singh, R. Venkatesh, Bhawna Sahni, A. K. Yadav, S. N. Jha, D. Bhattacharyya, P. D. Babu, K. G. Suresh, and Aftab Alam, CoFeVSb: A promising candidate for spin valve and thermoelectric applications, Phys. Rev. B **105**, 144409 (2022).

[22] Tanja Graf, Claudia Felser, and Stuart S. P. Parkin, Simple rules for the understanding of Heusler compounds, Prog. Solid State Chem. **39**, 1 (2011).

[23] K. Özdoğan, E. Şaşıoğlu, and I. Galanakis, Slater-Pauling behavior in LiMgPdSn-type multifunctional quaternary Heusler materials: Half-metallicity, spin-gapless and magnetic semiconductors, J. Appl. Phys. **113**, 193903 (2013).

[24] Nan Zheng and Yingjiu Jin, Band-gap and Slater-Pauling rule in half-metallic Ti_2-based Heusler alloys: A first-principles study, J. Magn. Magn. Mater. **324**, 3099 (2012).

[25] A. Karmakar, S. Majumdar, S. Kundu, T. K. Nath, and S. Giri, A Griffiths-like phase in antiferromagnetic $R_{0.5}Eu_{0.5}MnO_3$ (R = Pr, Nd, Sm), J. Phys.: Condens. Matter **25**, 066006 (2013).

[26] M. B. Salamon, P. Lin, and S. H. Chun, Colossal Magnetoresistance Is a Griffiths Singularity, Phys. Rev. Lett. **88**, 197203 (2002).

[27] A. J. Bray, Nature of the Griffiths Phase, Phys. Rev. Lett. **59**, 586 (1987).

[28] Robert B. Griffiths, Nonanalytic Behavior Above the Critical Point in a Random Ising Ferromagnet, Phys. Rev. Lett. **23**, 17 (1969).

[29] Shubhra Dash, A. V. Lukoyanov, Durgamadhab Mishra, U. P. Mohammed Rasi, R. B. Gangineni, M Vasundhara, and Ajit K. Patra, Structural stability and magnetic properties of Mn_2FeAl alloy with a β-Mn structure, J. Magn. Magn. Mater. **513**, 167205 (2020).

[30] Yuetong Qian, Meng Wu, Litao Yu, Hongwei Liu, Xiaodong Si, Xiaojing Luo, Zhe Li, Chuanbing Cai, and Yongsheng Liu, Griffiths phase and spontaneous magnetization in polycrystalline $Co_{50}V_{34}Ga_{16}$ alloy, J. Alloys Compd. **870**, 159421 (2021).

[31] Jie Chen, Hang Li, Bei Ding, Hongwei Zhang, Enke Liu, and Wenhong Wang, Large anomalous Hall angle in a topological semimetal candidate TbPtBi, Appl. Phys. Lett. **118**, 031901 (2021).

[32] M. Lee, T. F. Rosenbaum, M.-L. Saboungi, and H. S. Schnyders, Band-Gap Tuning and Linear Magnetoresistance in the Silver Chalcogenides, Phys. Rev. Lett. **88**, 066602 (2002).

[33] Charles Kittel, Introduction to Solid State Physics (2007), 7th ed.

[34] Michelle E. Jamer, Yung Jui Wang, Gregory M. Stephen, Ian J. McDonald, Alexander J. Grutter, George E. Sterbinsky, Dario A. Arena, Julie A. Borchers, Brian J. Kirby, Laura H. Lewis, Bernardo Barbiellini, Arun Bansil, and Don Heiman, Compensated Ferrimagnetism in the Zero-Moment Heusler Alloy Mn_3Al, Phys. Rev. Appl. **7**, 064036 (2017).

[35] K. Ahilan, M. C. Bennett, M. C. Aronson, N. E. Anderson, P. C. Canfield, E. Munoz-Sandoval, T. Gortenmulder, R. Hendrikx, and J. A. Mydosh, Magnetotransport in single-crystal half-Heusler compounds, Phys. Rev. B **69**, 245116 (2004).

[36] K. Kudo, A. Masago, S. Yamada, L. S. R. Kumara, H. Tajiri, Y. Sakuraba, K. Hono, and K. Hamaya, Positive linear magnetoresistance effect in disordered $L2_1$B-type Mn_2CoAl epitaxial films, Phys. Rev. B **103**, 104427 (2021).

[37] A. A. Abrikosov, Quantum magnetoresistance, Phys. Rev. B **58**, 2788 (1998).

[38] R. Xu, A. Husmann, T. F. Rosenbaum, M.-L. Saboungi, J. E. Enderby, and P. B. Littlewood, Large magnetoresistance in non-magnetic silver chalcogenides, Nature **390**, 57 (1997).

[39] T. Suzuki, R. Chisnell, A. Devarakonda, Y.-T. Liu, W. Feng, D. Xiao, Jeffrey W. Lynn, and J. G. Checkelsky, Large anomalous Hall effect in a half-Heusler antiferromagnet, Nat. Phys. **12**, 1119 (2016).

[40] Satoru Nakatsuji, Naoki Kiyohara, and Tomoya Higo, Large anomalous Hall effect in a non-collinear antiferromagnet at room temperature, Nature **527**, 212 (2015).

[41] Ajaya K. Nayak, Julia Erika Fischer, Yan Sun, Binghai Yan, Julie Karel, Alexander C. Komarek, Chandra Shekhar, Nitesh Kumar, Walter Schnelle, Jürgen Kübler, Claudia Felser, and Stuart S. P. Parkin, Large anomalous Hall effect driven by a nonvanishing Berry curvature in the noncolinear antiferromagnet Mn_3Ge, Sci. Adv. **2**, e1501870 (2016).

[42] Hiroshi Takatsu, Gwilherm Nénert, Hiroaki Kadowaki, Hideki Yoshizawa, Mechthild Enderle, Shingo Yonezawa, Yoshiteru Maeno, Jungeun Kim, Naruki Tsuji, Masaki Takata, Yang Zhao, Mark Green, and Collin Broholm, Magnetic structure of the conductive triangular-lattice antiferromagnet $PdCrO_2$, Phys. Rev. B **89**, 104408 (2014).

[43] Yufan Li, N. Kanazawa, X. Z. Yu, A. Tsukazaki, M. Kawasaki, M. Ichikawa, X. F. Jin, F. Kagawa, and Y. Tokura, Robust Formation of Skyrmions and Topological Hall Effect Anomaly in Epitaxial Thin Films of MnSi, Phys. Rev. Lett. **110**, 117202 (2013).

[44] K. Ueda, S. Iguchi, T. Suzuki, S. Ishiwata, Y. Taguchi, and Y. Tokura, Topological Hall Effect in Pyrochlore Lattice with Varying Density of Spin Chirality, Phys. Rev. Lett. **108**, 156601 (2012).

[45] Abhishek Singh, Vinod K. Gangwar, Prashant Shahi, Debarati Pal, Rahul Singh, Shiv Kumar, S. Singh, S. K. Gupta, Sudhir Kumar, Jinguang Cheng, and Sandip Chatterjee, Anomalous and topological Hall effect in Cu doped Sb_2Te_3 topological insulator, Appl. Phys. Lett. **117**, 092403 (2020).

[46] Wenbo Wang, Yi-Fan Zhao, Fei Wang, Matthew W. Daniels, Cui-Zu Chang, Jiadong Zang, Di Xiao, and Weida Wu, Chiral-bubble-induced topological Hall effect in ferromagnetic topological insulator heterostructures, Nano Lett. **21**, 1108 (2021), pMID: 33404255,

[47] Mal-Soon Lee and S. D. Mahanti, Validity of the rigid band approximation in the study of the thermopower of narrow band gap semiconductors, Phys. Rev. B **85**, 165149 (2012).

[48] Maxime Markov, S. Emad Rezaei, Safoura Nayeb Sadeghi, Keivan Esfarjani, and Mona Zebarjadi, Thermoelectric properties of semimetals, Phys. Rev. Mater. **3**, 095401 (2019).

[49] F. Garmroudi, A. Riss, M. Parzer, N. Reumann, H. Müller, E. Bauer, S. Khmelevskyi, R. Podloucky, T. Mori, K.

Tobita, Y. Katsura, and K. Kimura, Boosting the thermoelectric performance of Fe_2VAl-type Heusler compounds by band engineering, Phys. Rev. B **103**, 085202 (2021).

[50] H. B. Nielsen and M. Ninomiya, A no-go theorem for regularizing chiral fermions, Phys. Lett. B **105**, 219 (1981).

[51] Satya N. Guin, Qiunan Xu, Nitesh Kumar, Hsiang-Hsi Kung, Sydney Dufresne, Congcong Le, Praveen Vir, Matteo Michiardi, Tor Pedersen, Sergey Gorovikov, Sergey Zhdanovich, Kaustuv Manna, Gudrun Auffermann, Walter Schnelle, Johannes Gooth, Chandra Shekhar, Andrea Damascelli, Yan Sun, and Claudia Felser, 2D-Berry-curvature-driven large anomalous Hall effect in layered topological nodal-line MnAlGe, Adv. Mater. **33**, 2006301 (2021).

[52] K Kim, J Seo, E Lee, K. T. Ko, B. S. Kim, and G Bo, Large anomalous Hall current induced by topological nodal lines in a ferromagnetic van der Waals semimetal, Nat. Mater. **17**, 794 (2018).